

Superconducting praseodymium superhydrides

Di Zhou¹, Dmitrii V. Semenov², Defang Duan¹, Hui Xie¹, Wuha Chen¹, Xiaoli Huang^{1,*}, Xin Li¹,
Bingbing Liu¹, Artem R. Oganov^{2,3,*} and Tian Cui^{1,*}

¹ State Key Laboratory of Superhard Materials, College of Physics, Jilin University, Changchun 130012, China

² Skolkovo Institute of Science and Technology, Skolkovo Innovation Center 143026, 3 Nobel Street, Moscow, Russia

³ International Center for Materials Discovery, Northwestern Polytechnical University, Xi'an, 710072, China

*Corresponding authors: huangxiaoli@jlu.edu.cn, a.oganov@skoltech.ru and cuitian@jlu.edu.cn

ABSTRACT

Superhydrides have complex hydrogenic sublattices and are important prototypes for studying metallic hydrogen and high-temperature superconductors. Encouraged by the results on LaH₁₀, in consideration of the differences between La and Pr, Pr-H system is especially worth studying because of the magnetism and valence-band *f-electrons* in element Pr. Here we successfully synthesized praseodymium superhydrides (PrH₉) in laser-heated diamond anvil cells. Synchrotron X-ray diffraction (XRD) analysis demonstrated the presence of previously predicted $F\bar{4}3m$ -PrH₉ and unexpected $P6_3/mmc$ -PrH₉ phases. Moreover, $Fm\bar{3}m$ -PrH₃, $P4/nmm$ -PrH_{3- δ} and $Fm\bar{3}m$ -PrH_{1+x} were found below 52 GPa. $F\bar{4}3m$ -PrH₉ and $P6_3/mmc$ -PrH₉ were stable above 100 GPa in experiment. Experimental studies of electrical resistance in the PrH₉ sample showed the emergence of superconducting transition (T_c) below 9 K **and a dependent T_c on applied magnetic field**. Theoretical calculations indicate that magnetic order and electron-phonon interaction coexist in a very close range of pressures in the PrH₉ sample which may contribute to its low superconducting temperature T_c . Our results highlight the intimate connections among hydrogenic sublattices, density of states, magnetism and superconductivity in Pr-based superhydrides.

Keywords: high pressure, superhydrides, crystal structure, superconductivity

SUMMARY

Observations of high-temperature superconductivity in dense hydrogen-rich compounds have reinvigorated the field of high pressure and superconductivity ever since the striking discovery of H₃S and LaH₁₀ with T_c exceeding 200 K. Superhydrides with complex hydrogenic sublattices are important prototype systems to investigate metallization of hydrogen with potential high-temperature superconductivity. The present systematic experimental and computational study of the praseodymium hydrides reveals two phases of praseodymium superhydride (PrH₉) with intriguing crystal structures and properties under pressure. Our experimental results show that superconductivity declines along the La-Ce-Pr series, while magnetism becomes more and more pronounced, indicating that lanthanide atoms play a more profound role in determining superconducting T_c .

INTRODUCTION

The idea that hydrogen-rich compounds may be potential high- T_c superconductors that can be traced back to 2004 (1), when chemical pre-compression of hydrogen due to bonding with other elements was proposed as an effective way to reduce the metallization pressure of hydrogen. Recent experimental results of T_c exceeding 200 K in compressed H_3S (2, 3, 4) and 250-260 K in LaH_{10} system (5, 6, 7, 8) have indicated compressed hydrogen-rich compounds **toward** as potential room-temperature superconductors.

It is recognized that superconductivity in such hydrides owes its origin to electron-phonon coupling. According to BCS theory, from the expression of the critical temperature, three parameters determine T_c : the characteristic phonon frequency, electron-phonon coupling and Coulomb pseudo-potential (9). Recent theoretical studies have covered almost all binary hydrides, and found several metal superhydrides with extraordinary high- T_c superconductivity, such as CaH_6 (10), MgH_6 (11), YH_{6-10} (12, 13), AcH_{10-16} (14), ThH_{9-10} (15). Peng et al. (16) firstly studied all the candidate structures of rare earth superhydrides with H-rich cages at high pressure, and proposed that only several hydrides could be superconductors with $T_c > 77$ K. At the same time, superhydrides with H_2 units are recognized to have relatively low critical temperature, e.g. LiH_6 (17), NaH_7 (18), $Xe(H_2)_7$ (19) and $HI(H_2)_{13}$ (20). The question is why some superhydrides are high- T_c superconductors, while others, with the same structure and stoichiometry, are not.

Continuing studies of lanthanide superhydrides, in this work we studied high-pressure behavior of the Pr-H system above 100 GPa. Chesnut and Vohra (21) studied the crystal structure of metallic Pr and determined the phase sequence above megabar pressure. Pr can readily absorb hydrogen at high temperature and form hydrides: face-centered cubic dihydride PrH_2 and hexagonal close-packed trihydride PrH_3 were found at ambient pressure. Subsequent filling of octahedral voids in the structure of dihydrides leads to non-stoichiometric PrH_{2+x} composition which exhibit considerable variations of magnetic structures (22). Here, through high-pressure and high-temperature (HPHT) synthesis, two unexpected Pr superhydrides were obtained and studied. In particular, we investigated superconducting behavior of synthesized Pr superhydrides by electrical resistance measurements. Theoretical calculations are employed to deeply unearth the relationship among their magnetic properties, electronic band structures, phonon spectra and superconductivity. Comparison with already detailed studies of La and Ce superhydrides allows us to elucidate the great influence of metal atoms on superconductivity of superhydrides.

RESULTS AND DISCUSSION

The stability and structures predicted by theoretical calculations

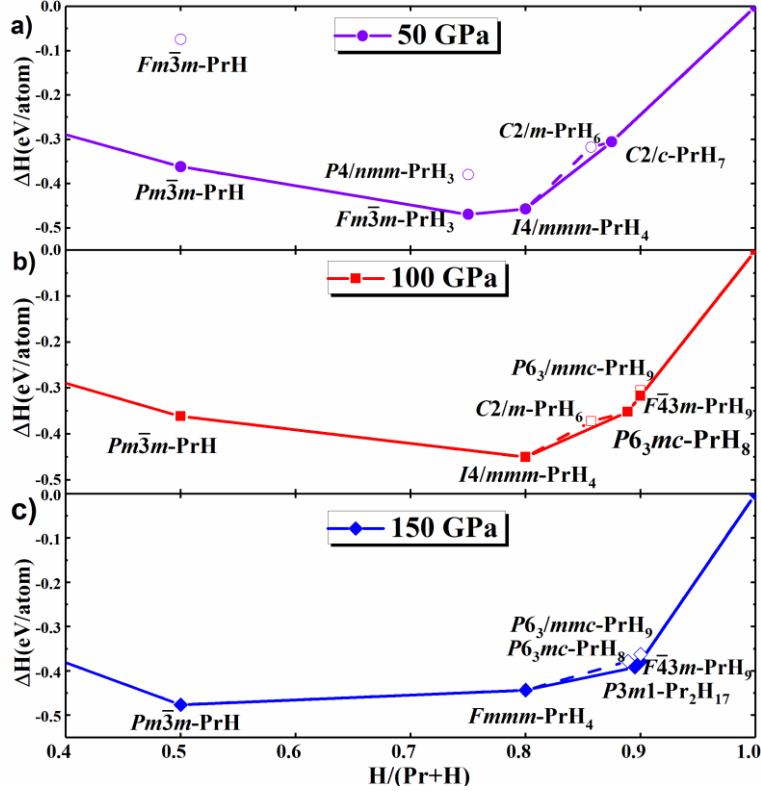


Fig. 1. Calculated convex hulls for Pr-H system at various pressures. Convex hulls for Pr-H system with spin-orbit coupling (SOC) and magnetic corrections at (a) 50 GPa, (b) 100 GPa and (c) 150 GPa.

Before describing the experimental results, we have compared our theoretical findings with the previous *ab initio* study (16), which is different from ours in a number of aspects. These differences are crucial for understanding our experimental results, and motivated us to further perform independent variable-composition searches for stable compounds in the Pr-H system at pressures of 50, 100 and 150 GPa using the USPEX (23, 24, 25) package and AIRSS (26) code (see Supplementary Materials Fig. S1). The current theoretical results performed by VASP (27, 28, 29) are also checked by an independent code CASTEP (30). The results of CASTEP can be found in Supplementary Materials Fig. S1. These two codes give the same results in principle. The only difference is the symmetry of PrH₃ that CASTEP gives $C2/m$ -PrH₃ while VASP gives $Pm\bar{3}m$ -PrH₃ without magnetism and spin-orbit coupling (SOC) effects.

Results of the structure search exhibit large differences depending on including or excluding magnetism and SOC effects, which can be seen in Fig. 1 and Supplementary Materials Fig. S1. However, previous calculations (16) didn't include these effects. In agreement with previous results (16) our search gives $Pm\bar{3}m$ as the most stable symmetry for monohydride PrH and $Fm\bar{3}m$ for trihydride PrH₃, but, such important metastable phases for the further $P4/nmm$ -PrH₃ (~ 70 meV/atom above the convex hull) and $Fm\bar{3}m$ -PrH were not reported. Previous work indicated that superhydride $F\bar{4}3m$ -PrH₉ is stable between 100 and 200 GPa, but no $P6_3/mmc$ -PrH₉, which is about 19 meV/atom above the convex hull at 100 GPa. We also updated the convex hull and phase diagram of Pr-H system at 150 GPa.

Synthesis of polyhydrides $Fm\bar{3}m\text{-PrH}_3$ and $P4/nmm\text{-PrH}_{3-\delta}$

To synthesize novel hydrides, we carried out several experiments by directly compressing Pr and hydrogen in the DACs. The diamond used in this experiment was coated with 150 nm alumina film by magnetron sputtering. The metallic Pr sample was loaded and sealed with a little pressure in the argon-protected glove box. After loading hydrogen into the cell, the sealed pressure was about 10 GPa, and selected XRD patterns are shown at various pressure (see Supplementary Materials Fig. S3c). Before laser heating, the diffraction pattern at 30 GPa included peaks from $Fm\bar{3}m\text{-PrH}_3$ in Fig. 2a, the structure of which can be viewed as cubic close packing of Pr atoms with all octahedral and tetrahedral voids filled by H atoms. (see Fig. 2c). After compression to 40 GPa, the sample was laser-heated to 1400 K. We found stronger signal from $Fm\bar{3}m\text{-PrH}_3$, while peaks from $Fm\bar{3}m\text{-PrH}$ disappeared (see Supplementary Materials Fig. S3c). Upon further compression, the diamonds were broken.

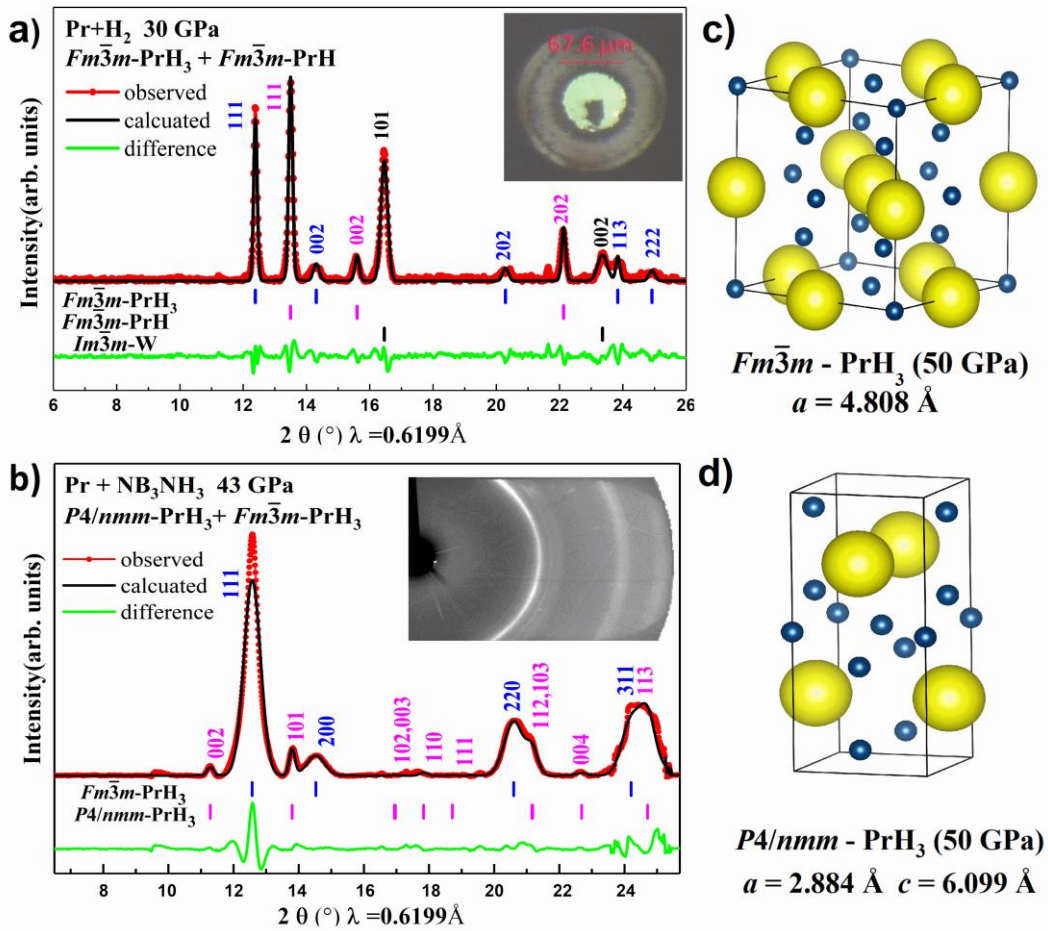


Fig. 2. XRD patterns and crystal structures of PrH₃ at pressures. (a) Refinement of the experimental XRD patterns obtained in Pr + H₂ cell by cold compression to 30 GPa. (b) Refinement of the XRD pattern by $Fm\bar{3}m\text{-PrH}_3$ and $P4/nmm\text{-PrH}_3$ after laser-heating at 43 GPa. Red line: experimental data; black line: model fit for the structure; green line: residues. Reliable parameters for the refinement are $R_p = 14.2 \%$, $R_{wp} = 24.5 \%$. Crystal structures of (c) $Fm\bar{3}m\text{-PrH}_3$ and (d) $P4/nmm\text{-PrH}_3$ phase at 50 GPa.

The experimental volumes of cubic PrH₃ are in good agreement with the predicted $Fm\bar{3}m\text{-PrH}_3$ structure in the pressure range 10-53 GPa (see Fig. 3b). The experimental equation of state (EoS) of this phase was fitted by the third-order Birch-Murnaghan equation of state (3rd B-M), which gave $V_0 = 37.7 (3) \text{ \AA}^3$, $K_0 = 113 (2)$

GPa, and $K_0' = 3.0$ (5). $Fm\bar{3}m$ -PrH, proposed for explanation of the XRD pattern, is slightly non-stoichiometric from the EoS (Fig.3c), it seems more correct to define as $Fm\bar{3}m$ -PrH_{1+x} where $x = 0.08 - 0.13$.

It is well known that experimental studies of hydrides are greatly affected by the hydrogen permeability contributing to the failure of the high-pressure experiments. To minimize this problem, we synthesized the new hydrides by replacing of pure hydrogen with ammonia borane (AB), which is an excellent source of hydrogen (released during decomposition of AB). Several experiments were performed according to the reaction: $\text{Pr} + \text{NH}_3\text{BH}_3 \rightarrow \text{PrH}_x + c\text{-BN}$ through HPHT treatment (31, 32, 33). Fig. 2b shows the diffraction pattern after laser heating at 43 GPa. The reacted products are mainly dominated by $Fm\bar{3}m$ -PrH₃ with a small quantity of tetragonal phase $P4/nmm$ -PrH_{3- δ} ($0.05 \leq \delta \leq 0.15$) with smaller unit cell volume. At 50 GPa in the $P4/nmm$ -PrH₃ structure, each Pr atom is linked with 9 H atoms with $2.09 \text{ \AA} \leq d(\text{Pr-H}) \leq 2.17 \text{ \AA}$. Experimental cell parameters of discovered compounds are shown in Supplementary Materials Table S3.

Synthesis of $F\bar{4}3m$ -PrH₉ and $P6_3/mmc$ -PrH₉

To obtain higher hydrides of Pr, we conducted further experiments at pressures above 100 GPa. To overcome problems with hydrogen permeation, we also used NH₃BH₃ (AB) as the source of hydrogen, which proved to be effective for synthesis of superhydrides at megabar pressures (7, 34). The original sample containing Pr with AB was laser-heated to 1650 K at 115 GPa. Measurements after laser-heating did not show any changes in pressure, and Raman signal of H₂ was detected at 4147 cm⁻¹, indicating the generation of hydrogen. Fig. 3a shows the XRD pattern with the presence of two praseodymium superhydrides $F\bar{4}3m$ -PrH₉ and $P6_3/mmc$ -PrH₉. Experimental lattice parameters at 120 GPa are $a = 4.967$ (1) Å, $V = 122.52$ (9) Å³ for $F\bar{4}3m$ -PrH₉ and $a = 3.588$ (1) Å, $c = 5.458$ (4) Å, $V = 60.84$ (9) Å³ for $P6_3/mmc$ -PrH₉. This sample was compressed to 130 GPa and then gradually decompressed down to the lowest pressure 105 GPa to determine its experimental equation of state (Fig. 3b, Table S4). Both EoS of PrH₉ are very close to the calculated curve of Pr+9H and correspond well with the calculated values. After decompression, the cell dropped down to 53 GPa, and recorded XRD pattern demonstrates the presence of two lower hydride phases: $Fm\bar{3}m$ -PrH₃ with experimental parameters of $a = 4.832$ (1) Å at 50 GPa, and $P4/nmm$ -PrH_{3- δ} with $a = 2.801$ (1) Å, $c = 6.280$ (2) Å at 50 GPa, which is consistent with the low pressure results.

Both structures have almost the same volume and energy on convex hull at studied pressure range (Fig. 1b-1c). It is interesting to note that stability of $F\bar{4}3m$ -PrH₉ was previously predicted (16), while its coexistence with metastable $P6_3/mmc$ -PrH₉ is a surprise. According to our theoretical calculations, the enthalpy difference between $P6_3/mmc$ -PrH₉ and $F\bar{4}3m$ -PrH₉ is about 19 meV/atom which is near the limit of DFT accuracy. According to recent studies (35, 36), 20% of experimentally synthesized materials are metastable, some of which even have high positive.

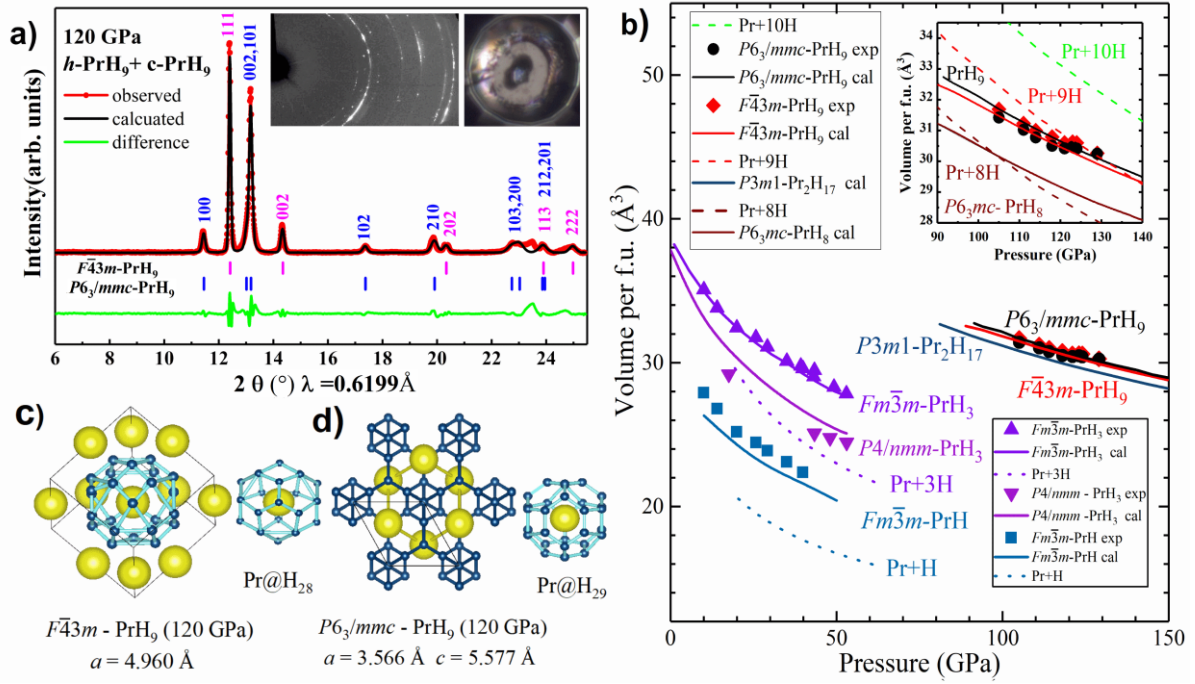


Fig. 3. Refinement of the experimental XRD pattern, pressure-volume data and crystal structure of PrH₉. (a) Refinement of the XRD pattern by $F\bar{4}3m$ -PrH₉ and $P6_3/mmc$ -PrH₉. Red line: experimental data; black line: model fit for the structure; green line: residues. Reliable parameters are as $R_p = 12.4\%$, $R_{wp} = 22.0\%$. (b) EoS of the synthesized Pr-H phases; theoretical results include magnetism and SOC effects. Inset: the distinction among PrH₈, PrH₁₀ and PrH₉ phases. Crystal structures of (c) $F\bar{4}3m$ -PrH₉ with H₂₈ cages and (d) $P6_3/mmc$ -PrH₉ with H₂₉ cages.

Properties of $F\bar{4}3m$ -PrH₉ and $P6_3/mmc$ -PrH₉

We performed a series of experiments to investigate superconductivity of PrH₉ via measurements of electrical resistance $R(T)$ in the range of 1.6 to 300 K at pressures from 100 GPa up to 150 GPa. The XRD pattern of the prepared sample at 126 GPa deposited with four electrodes, shows presence of both $F\bar{4}3m$ -PrH₉ and $P6_3/mmc$ -PrH₉ phases (Fig. 4c). Possible superconducting transitions were detected with the resistance drop below 9 K, so we proposed that the superconducting transition temperature is below 9 K, far below LaH₁₀ of the same main group. The superconducting resistance drop $R(T)$ is also dependent on applied magnetic field, further proving this is a superconducting transition (see Fig. 4d). Another run of experiments confirmed the existence of the pronounced superconducting resistance drop in PrH₉ below 9 K (see Fig. 4e and Supplementary Materials Fig. S9). The complexity of the experiments prevented us from accurately determining the pressure dependence of superconducting T_c . We did not observe zero resistance of the superhydrides samples because of their complex geometries, and the samples were clearly mixed phase, possible with varying hydrogen stoichiometry. The same phenomena of incompletely dropping to zero in resistance have also been reported in the measurement of superconducting resistance of boron (37) and iron (38) at high pressure.

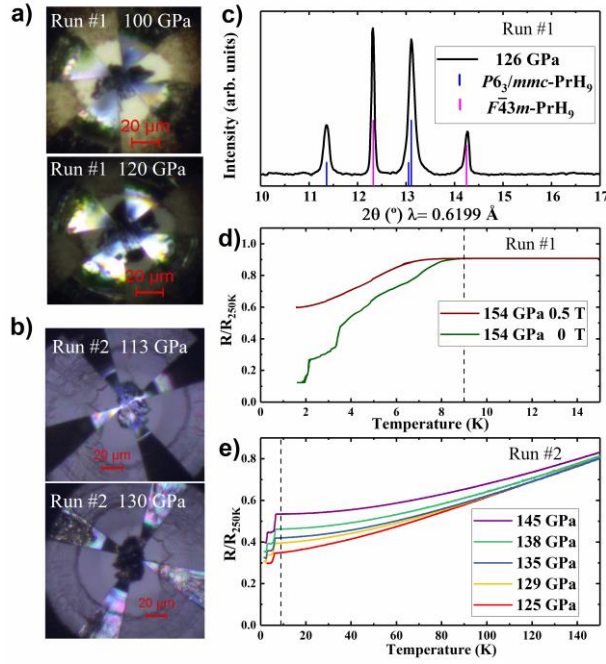


Fig. 4. Electrical resistance measurements of PrH₉. (a) The sample inside the diamond anvil cell connected with four electrodes before and after laser heating for sample 1. (b) The photos of sample 2 from different sides of cell after heating. (c) XRD pattern proves the cubic and hexagonal PrH₉ were synthesized in the sample at around 120 GPa from a mixture of Pr and AB. (d) Resistance steps of sample 1 at different magnetic field. (e) Resistance steps of sample 2 at different pressure.

Further theoretical calculations try to understand why both $F\bar{4}3m$ -PrH₉ and $P6_3/mmc$ -PrH₉ possess such low T_c . As shown in Fig. 3c-3d, both structures have clathrate structures, which are also found in other rare earth hydrides. Calculations of the electron localization function (ELF) reveal weak covalent H-H interactions. In $F\bar{4}3m$ -PrH₉ structure, the nearest H-H distance is 1.135 Å at 120 GPa, which is a bit longer than the known shortest H-H distance in $P6_3/mmc$ -CeH₉ (~ 1.1 Å) (39), but shorter than $Fm\bar{3}m$ -LaH₁₀ (5). At the same time, $P6_3/mmc$ -PrH₉ with Pr@H₂₉ cages has the nearest H-H distance of ~1.170 Å (at 120 GPa), which is longer than $d_{\min}(\text{H-H})$ in atomic hydrogen as well as in CeH₉ at the same pressure (16) (for details see Fig. S4).

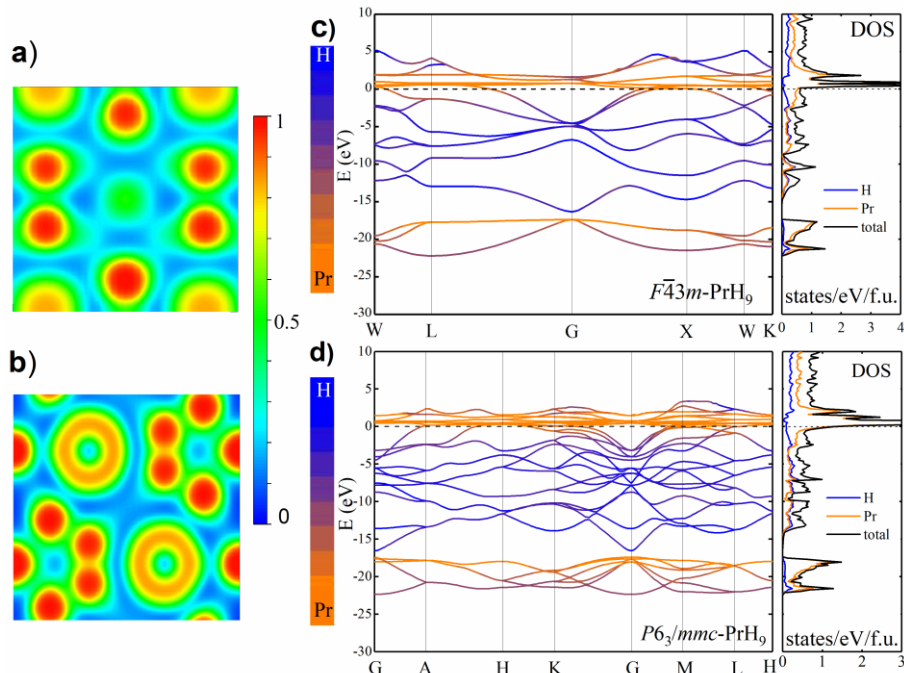


Fig. 5. Electronic properties of PrH₉. Electron localization function (ELF) of (a) $F\bar{4}3m$ -PrH₉ and (b) $P6_3/mmc$ -PrH₉. Calculated densities of electron states (DOS) and band structure in (c) $F\bar{4}3m$ -PrH₉ and (d) $P6_3/mmc$ -PrH₉ at 150 GPa.

DOS (E_F) is mostly due to *f-electrons* of Pr and has very high value in both cases.

Calculations demonstrate that both PrH₉ structures are dynamically stable (Fig. S6) and exhibit metallic properties (Fig. 5). But only 6 to 9 % of the total DOS comes from the hydrogen atoms, the rest being due to *f-electrons* of Pr. Relatively high values of the density of states above 3-4 eV⁻¹f.u.⁻¹ at or near (± 1 eV) the Fermi level caused by a series of Van Hove singularities, make it impossible to use constant DOS approximation when calculating parameters of the superconducting state in PrH₉ (40). Low contribution of hydrogen to DOS is associated with weak electron-phonon coupling (EPC) at 150 GPa, resulting in low superconducting T_c . EPC calculations for both PrH₉ with the selected PP give the estimated T_c of 0.8 K for cubic PrH₉ and 8.4 K for hexagonal PrH₉ at 120 GPa with $\mu^* = 0.1$, which is good agreement with experiments (see Supplementary materials, Fig. S10 - S12).

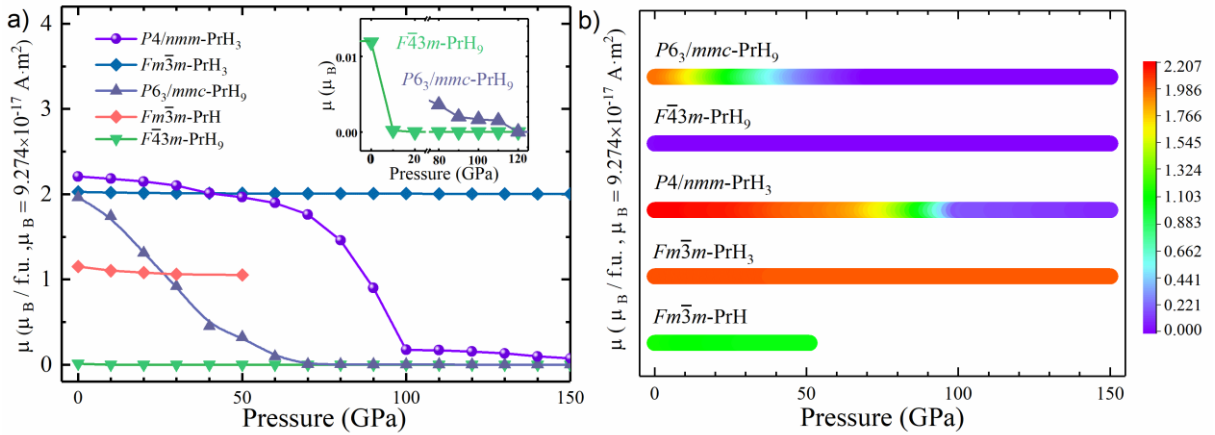


Fig. 6. Magnetism of Pr hydrides at pressures up to 150 GPa. (a) Magnetic moments of Pr-H system at high pressure and (b) Magnetic map of Pr-H system as a function of pressure.

We summarized magnetic properties for all studied praseodymium hydrides at pressure range 0-150 GPa in Fig. 6. We find that all Pr-H compounds are magnetic: $Fm\bar{3}m\text{-PrH}_3$ and $Fm\bar{3}m\text{-PrH}$ possess strong magnetism and retain almost constant magnetic moments at high pressures, while tetragonal PrH₃ and both phases of PrH₉ lose magnetism under pressure. $P6_3/mmc\text{-PrH}_9$ loses magnetism at 120 GPa, while $F\bar{4}3m\text{-PrH}_9$ retains a very low magnetic moment. Magnetic order and electron-phonon interaction coexist in a very close range of pressures in praseodymium hydrides which may have an effect on the low superconducting transition temperature T_c .

CONCLUSIONS

By the efficient means of *in situ* decomposition reaction of NH₃BH₃ under HPHT conditions previously used for synthesis of lanthanum superhydrides, we synthesized two novel metallic superhydrides $F\bar{4}3m\text{-PrH}_9$ and $P6_3/mmc\text{-PrH}_9$, two trihydrides $Fm\bar{3}m\text{-PrH}_3$ and $P4/nmm\text{-PrH}_{3-\delta}$, and one monohydride $Fm\bar{3}m\text{-PrH}_{1+x}$ in the pressure range 0 – 130 GPa. For most synthesized phases the equations of state and unit cell parameters are in good agreement with our DFT calculations. Resistance measurements of praseodymium hydrides indicated possible superconducting transitions in both PrH₉ were below 9 K, which is in agreement with theoretical calculations: 8.4 K for hexagonal and 0.8 K for cubic PrH₉ at 120 GPa. Magnetic order and

electron-phonon interaction coexist in a very close range of pressures in praseodymium hydrides which may have an effect on the low superconducting transition temperature. Present results on Pr superhydrides show that superconductivity declines along the La-Ce-Pr series, while magnetism becomes more and more pronounced. Metallic atoms are not just donors of the electrons to the “metallic hydrogen” sublattice, but play a more profound role in determining superconducting T_c .

METHODS

Experimental method: The praseodymium powder samples were purchased from Alfa Aesar with a purity of 99.99%. Molybdenum electrodes were sputtered onto the surface of one diamond anvils in the van der Pauw four-probe geometry. A four-probe measurement scheme was essential to separate the sample signal from the parasitic resistance of the current leads. We prepared an isolated layer from cubic boron nitride (or a mixture of epoxy and CaF_2). We performed laser heating of three diamond anvil cells (100 μm and 150 μm culets) loaded with metallic Pr sample and ammonia borne in the argon-protected glove box. The diamonds used for electrical DACs had a culet with a diameter of 100 μm . Thickness of the tungsten gasket was 20 ± 2 μm . Heating was carried out by pulses of infrared laser with wavelength 1 μm (Nd:YAG) and temperature measurements were carried out by the MAR 345 detector. Applied pressure was measured by the edge position of diamond Raman signal (41). X-ray diffraction patterns studied in diamond anvil cells samples were recorded on the BL15U1 synchrotron beamline (42) at Shanghai Synchrotron Research Facility (SSRF, China) with the use of a focused (5×12 μm) monochromatic. Additional syntheses with electrodes were carried out at the 4W2 High-Pressure Station of Beijing Synchrotron Radiation Facility (BSRF, China). The beam size was about 32×12 μm . both facilities are with the incident X-ray beam (20 keV, 0.6199 \AA) and a Mar165 CCD two-dimensional as the detector. The experimental X-ray diffraction images were analyzed and integrated using the Dioptas software package (43). The full profile analysis of the diffraction patterns, as well as the calculation of the unit cell parameters, was performed in the Materials studio (44) and JANA2006 program (45) by the Le Bail method (46).

Theoretical calculations: We have carried out variable-composition searches for stable compounds in the Pr-H system at pressures of 50, 100 and 150 GPa using the USPEX (23, 24, 25) package and AIRSS (26) code coupled with the Cambridge serial total energy package (CASTEP) plane-wave code (30) and on the fly pseudopotentials (47). The first generation of USPEX search (120 structures) was created using a random symmetric generator, while all subsequent generations (100 structures) contained 20% random structures and 80% created using heredity, softmutation, and transmutation operators.

We calculated the equation of states (EoS) for PrH, both PrH_3 and two PrH_9 phases. In order to calculate the equations of state, we performed structure relaxations of phases at various pressures using density functional theory (DFT) (48, 49) within the generalized gradient approximation (Perdew-Burke-Ernzerhof functional) (50, 51) and the projector-augmented wave method (52, 53) as implemented in the VASP code

(27, 28, 29). Plane wave kinetic energy cutoff was set to 1000 eV and the Brillouin zone was sampled using Γ -centered k -points meshes with resolution $2\pi \times 0.05 \text{ \AA}^{-1}$. Obtained dependences of the unit cell volume on pressure were fitted by three-order Birch-Murnaghan equation (54) to determine the main parameters of the EoS, namely V_0 , K_0 and K' , where V_0 is equilibrium volume, K_0 is bulk modulus and K' is derivative of bulk modulus with respect to pressure using the EoSfit7 software (55). We also calculated phonon densities of states for studied materials using finite displacement method (VASP (56) and PHONOPY (57)).

Calculations of phonons, electron-phonon coupling and superconducting T_c were carried out with QUANTUM ESPRESSO (QE) package (58) using density-functional perturbation theory (59), employing plane-wave pseudopotential method and local-density approximation exchange-correlation functional (60). Norm-conserving potentials for H ($1s^1$) and Pr ($5s^2 5p^6 4f^3 6s^2$) were used with a kinetic energy cutoff of 90 Ry. In our *ab initio* calculations of the electron-phonon coupling (EPC) parameter λ , the first Brillouin zone was sampled using a $6 \times 6 \times 6$ q -points mesh with a denser $24 \times 24 \times 24$ k -points mesh for $F\bar{4}3m$ -PrH₉, and a $3 \times 3 \times 2$ q -points mesh with a denser $15 \times 15 \times 10$ k -points mesh for $P6_3/mmc$ -PrH₉ (with Gaussian smearing and $\sigma = 0.035$ Ry which approximates the zero-width limits in the calculation of λ). Critical temperature T_c was calculated from the Allen-Dynes modified McMillan formula (61): $T_c = \frac{\omega_{log}}{1.2} \exp\left[-\frac{1.04(1+\lambda)}{\lambda - \mu^*(1+0.62\lambda)}\right]$, with $\omega_{log} = \exp\left[\frac{2}{\lambda} \int \ln(\omega) \frac{\alpha^2 F(\omega)}{\omega} d\omega\right]$ and $\lambda = 2 \int \frac{\alpha^2 F(\omega)}{\omega} d\omega$, where μ^* , $\alpha^2 F(\omega)$ and λ are Coulomb parameter, the electron-phonon spectral function and the EPC parameter.

SUPPLEMENTARY MATERAILS

Table S1 Crystal structure of predicted Pr-H phases.

Table S2 Experimental parameters of DACs.

Table S3 Experimental cell parameters and volumes of lower praseodymium hydrides along with calculated cell volumes (V_{DFT}).

Table S4 Experimental cell parameters and volumes of two praseodymium superhydrides along with calculated cell volumes (V_{DFT}).

Table S5 Reference EoS parameters of pure elemental Pr in Birch–Murnaghan equation.

Table S6 Calculated EoS parameters of 3rd Birch–Murnaghan equation for all studied Pr-H phases.

Fig. S1 Calculated convex hulls for Pr-H system at various pressures.

Fig. S2 Convex hulls without and with ZPE correction and crystal structure of discovered praseodymium hydrides at 120 GPa.

Fig. S3 Experimental XRD patterns dependence of pressure in the range of 0-130 GPa.

Fig. S4 (a) Comparison of the pressure dependence of the nearest H-H distances for two PrH₉, LaH₁₀, CeH₉, and atomic H. **(b)** Nearest Pr-H distances as a function of pressure calculated from experimental cell parameters.

Fig. S5 Raman spectra of Z1 cell under decompression.

Fig. S6 Calculated phonon density of states and band structure for $P6_3/mmc$ -PrH₉ **(a)** and $F\bar{4}3m$ -PrH₉ **(b)** at 120 GPa.

Fig. S7 Calculated phonon density of states and band structure for $P6_3mc$ -PrH₈ (a) at 120 GPa and $P4/nmm$ -PrH₃ at 50 GPa (b).

Fig. S8 Electron density of states for cubic PrH₃ and $P4/nmm$ -PrH₃ at 30 GPa.

Fig. S9 Enlarged figure of electrical resistance measurements of PrH₉ in sample 2.

Fig. S10 Calculated superconducting parameters of $F\bar{4}3m$ -PrH₉ at 120 GPa as a function of electronic smearing σ and the pseudopotential.

Fig. S11 Eliashberg spectral functions, the electron-phonon integral $\lambda(\omega)$ and critical transition temperature $T_c(\omega)$ calculated at 120 GPa for cubic PrH₉ with $\sigma = 0.035$ Ry.

Fig. S12 A series of Eliashberg spectral functions calculated at 120 GPa for hexagonal PrH₉.

REFERENCES AND NOTES

1. N. W. Ashcroft. Hydrogen dominant metallic alloys: high temperature superconductors? *Phys. Rev. Lett.* **92**, 187002-187001-187002-187004 (2004).
2. A. P. Drozdov, M. I. Eremets, I. A. Troyan, V. Ksenofontov, S. I. Shylin. Conventional superconductivity at 203 kelvin at high pressures in the sulfur hydride system. *Nature* **525**, 73-76 (2015).
3. M. Einaga *et al.* Crystal Structure of the Superconducting Phase of Sulfur Hydride. *Nat. Phys.* **12**, 835-838 (2016).
4. X. Huang *et al.* High-temperature Superconductivity in Sulfur Hydride Evidenced by Alternating-current Magnetic Susceptibility. *National Science Review* **nwz061**, (2019).
5. Z. M. Geballe *et al.* Synthesis and Stability of Lanthanum Superhydrides. *Angew. Chem. Int. Ed.* **129**, 6 (2017).
6. M. Somayazulu *et al.* Evidence for Superconductivity above 260 K in Lanthanum Superhydride. *arXiv:1808.07695*, (2018).
7. M. Somayazulu *et al.* Evidence for Superconductivity above 260 K in Lanthanum Superhydride. *Phys. Rev. Lett.* **122**, 027001 (2019).
8. A. P. Drozdov *et al.* Superconductivity at 250 K in lanthanum hydride under high pressures. *Nature* **569**, 528-531 (2019).
9. J. M. McMahon, D. M. Ceperley. High-temperature superconductivity in atomic metallic hydrogen. *Phys. Rev. B* **84** 144515 (2011).
10. H. Wang, J. S. Tse, K. Tanaka, T. Iitaka, Y. Ma. Superconductive sodalite-like clathrate calcium hydride at high pressures. *PNAS* **109**, 6463-6466 (2012).
11. X. Feng, J. Zhang, G. Gao, H. Liu, H. Wang. Compressed sodalite-like MgH₆ as a potential high-temperature superconductor. *RSC Advances* **5**, 59292-59296 (2015).
12. Y. Li, J. Hao, H. Liu, J. S. Tse, Y. Wang, Y. Ma. Pressure-stabilized superconductive yttrium hydrides. *Sci. Rep.* **5**, 9948 (2015).
13. H. Liu, I. I. Naumov, R. Hoffmann, N. W. Ashcroft, R. J. Hemley. Potential high-T_c superconducting lanthanum and yttrium hydrides at high pressure. *PNAS* **114**, 5 (2017).

14. D. V. Semenov, A. G. Kvashnin, I. A. Kruglov, A. R. Oganov. Actinium Hydrides AcH₁₀, AcH₁₂, and AcH₁₆ as High-Temperature Conventional Superconductors. *J. Phys. Chem. Lett.* **9**, 1920-1926 (2018).
15. A. G. Kvashnin, D. V. Semenov, I. A. Kruglov, I. A. Wrona, A. R. Oganov. High-Temperature Superconductivity in Th-H System at Pressure Conditions. *ACS Appl. Mater. Interfaces* **10**, 43809-43816 (2018).
16. F. Peng, Y. Sun, C. J. Pickard, R. J. Needs, Q. Wu, Y. Ma. Hydrogen Clathrate Structures in Rare Earth Hydrides at High Pressures: Possible Route to Room-Temperature Superconductivity. *Phys. Rev. Lett.* **119**, 107001 (2017).
17. C. Pépin, P. Loubeyre, F. Occelli, P. Duma. Synthesis of lithium polyhydrides above 130 GPa at 300 K. *PNAS* **112**, 7673-7676 (2015).
18. V. V. Struzhkin *et al.* Synthesis of sodium polyhydrides at high pressures. *Nat. Commun.* **7**, 12267 (2016).
19. M. Somayazulu *et al.* Pressure-induced bonding and compound formation in xenon–hydrogen solids. *Nat. Chem.* **2**, 50-53 (2009).
20. J. Binns, P. Dalladay-Simpson, M. Wang, G. J. Ackland, E. Gregoryanz, R. T. Howie. Formation of H₂ - rich iodine-hydrogen compounds at high pressure. *Phys. Rev. B* **97**, 024111 (2018).
21. G. N. Chesnut, Y. K. Vohra. Phase transformations and equation of state of praseodymium metal to 103 GPa. *Phys. Rev. B* **62**, 2965-2968 (2000).
22. P. Vajda, J. N. Daou. Rare Earths-Hydrogen. *Solid State Phenomena* **49-50**, 71-158 (1996).
23. A. R. Oganov, C. W. Glass. Crystal structure prediction using ab initio evolutionary techniques: Principles and applications. *J. Chem. Phys.* **124**, 244704 (2006).
24. A. R. Oganov, R. O. Lyakhov, M. Valle. How Evolutionary Crystal Structure Prediction Works-and Why. *Acc. Chem. Res.* **44**, 227-237 (2011).
25. A. O. Lyakhov, A. R. Oganov, H. T. Stokes, Q. Zhu. New developments in evolutionary structure prediction algorithm USPEX. *Computer Phys. Commun.* **184**, 1172-1182 (2013).
26. C. J. Pickard, R. J. Needs. Ab initio Random Structure Searching. *J. Phys.: Condens. Matter* **23**, 053201 (2011).
27. G. Kresse, J. Hafner. Ab initio molecular dynamics for open-shell transition metals. *Phys. Rev. B* **48**, 13115-13118 (1993).
28. G. Kresse, J. Hafner. Ab initio molecular-dynamics simulation of the liquid-metal–amorphous-semiconductor transition in germanium. *Phys. Rev. B* **49**, 14251-14269 (1994).
29. G. Kresse, J. Hafner. Efficient iterative schemes for ab initio total-energy calculations using a plane-wave basis set. *Phys. Rev. B* **54**, 11169 (1996).
30. S. J. Clark *et al.* First principles methods using CASTEP. *Zeitschrift für Kristallographie - Crystalline Materials* **220**, (2005).
31. R. S. Chellappa, M. Somayazulu, V. V. Struzhkin, T. Autrey, R. J. Hemley. Pressure-induced complexation of NH₃BH₃–H₂. *J. Chem. Phys.* **131**, 224515 (2009).

32. Y. Song. New perspectives on potential hydrogen storage materials using high pressure. *Phys. Chem. Chem. Phys.* **15**, 14524-14547 (2013).
33. R. G. Potter, M. Somayazulu, G. Cody, R. J. Hemley. High Pressure Equilibria of Dimethylamine Borane, Dihydridobis(dimethylamine)boron(III) Tetrahydridoborate(III), and Hydrogen. *The Journal of Physical Chemistry C* **118**, 7280-7287 (2014).
34. D. V. Semenov, A. G. Kvashnin, A. G. Ivanova, V. Svitlyk, I. A. Troayn, A. R. Oganov. Superconductivity at 161 K in Thorium Hydride ThH₁₀: Synthesis and Properties. *arXiv:1902.10206*, (2019).
35. Y. Wu, P. Lazic, G. Hautier, K. Persson, G. Ceder. First principles high throughput screening of oxynitrides for water-splitting photocatalysts. *Energy Environ. Sci.* **6**, 157 (2013).
36. Y. Hinuma *et al.* Discovery of earth-abundant nitride semiconductors by computational screening and high-pressure synthesis. *Nat. Commun.* **7**, 11962 (2016).
37. M. I. Eremets, V. V. Struzhkin, H.-k. Mao, R. J. Hemley. Superconductivity in Boron. *Science* **293**, 272 (2001).
38. K. Shimizu *et al.* Superconductivity in non-magnetic state of iron under pressure. *Nature* **412**, 316-318 (2001).
39. X. Li *et al.* Polyhydride CeH₉ with an atomic-like hydrogen clathrate structure. *Nat. Commun.* **10**, 3461 (2019).
40. W. Sano, T. Koretsune, T. Tadano, R. Akashi, R. Arita. Effect of Van Hove singularities on high-T_c superconductivity in H₃S. *Physical Review B* **93**, (2016).
41. M. I. Eremets. Megabar high-pressure cells for Raman measurements. *Journal of Raman Spectroscopy* **34**, 515-518 (2003).
42. L. L. Zhang *et al.* Hard X-ray micro-focusing beamline at SSRF. *NUCLEAR SCIENCE AND TECHNIQUES* **26**, 060101 (2015).
43. C. Prescher, V. B. Prakapenka. DIOPTAS: a program for reduction of two-dimensional X-ray diffraction data and data exploration. *High Pressure Research* **35**, 223-230 (2015).
44. R. A. Young. The Rietveld Method. *International union of crystallography* **5**, 1-38 (1993).
45. V. Petříček, M. Dušek, L. Palatinus. Crystallographic Computing System JANA2006: General features. *Z. Kristallogr.* **229**, 345-352 (2014).
46. A. L. Bail, H. Duroy, J. L. Forquet. Ab-initio structure determination of LiSbWO₆ by X-ray powder diffraction. *Mater. Res. Bull.* **23**, 447-452 (1988).
47. D. Vanderbilt. Soft self-consistent pseudopotentials in a generalized eigenvalue. *Phys. Rev. B* **41**, 7892–7895 (1990).
48. P. Hohenberg, W. Kohn. Inhomogeneous Electron Gas. *Phys. Rev.* **136**, B864-B871 (1964).
49. W. Kohn, L. J. Sham. Self-Consistent Equations Including Exchange and Correlation Effects. *Phys. Rev.* **140**, A1133-A1138 (1965).
50. J. P. Perdew, K. Burke, M. Ernzerhof. Generalized Gradient Approximation Made Simple. *Phys. Rev. Lett.* **77**, 3865-3868 (1996).

51. J. P. Perdew, K. Burke, M. Ernzerhof. Generalized Gradient Approximation Made Simple [Phys. Rev. Lett. 77, 3865 (1996)]. *Phys. Rev. Lett.* **78**, 1396 (1997).
52. P. E. Blöchl. Projector augmented-wave method. *Phys. Rev. B* **50**, 17953-17979 (1994).
53. G. Kresse, D. Joubert. From ultrasoft pseudopotentials to the projector augmented-wave method. *Phys. Rev. B* **59**, 1758 (1999).
54. B. Francis. Finite Elastic Strain of Cubic Crystals. *Phys. Rev.* **71**, 809-824 (1947).
55. J. Gonzalez-Platas, M. Alvaro, F. Nestola, R. Angel. EosFit7-GUI: a new graphical user interface for equation of state calculations, analyses and teaching. *J. Applied Crystallography* **49**, 1377-1382 (2016).
56. A. Togo, F. Oba, I. Tanaka. First-principles calculations of the ferroelastic transition between rutile-type and CaCl₂-type SiO₂ at high pressures. *Phys. Rev. B* **78**, 134106 (2008).
57. A. Togo, I. Tanaka. First principles phonon calculations in materials science. *Scripta Materialia* **108**, 1-5 (2015).
58. P. Giannozzi *et al.* QUANTUM ESPRESSO: a modular and open-source software project for quantum simulations of materials. *J. Phys.: Condens. Matter* **21**, 395502 (2009).
59. A. D. Becke. A new mixing of Hartree–Fock and local density-functional theories. *J Chem Phys* **98**, 1372-1377 (1993).
60. J. P. Perdew, A. Zunger. Self-interaction correction to density-functional approximations for many-electron systems. *Phys. Rev. B* **23**, 5048 (1981).
61. P. B. Allen, R. C. Dynes. Transition temperature of strong-coupled superconductors reanalyzed. *Phys. Rev. B* **12**, 905-922 (1975).
62. C. M. Pépin, G. Geneste, A. Dewaele, M. Mezouar, P. Loubeyre. Synthesis of FeH₅: A layered structure with atomic hydrogen slabs. *Science* **357**, 382 (2017).
63. K. Conder, J. Schefer, E. Kaldis, C. R. Xiu. Progress in the T-X Phase Diagram of the Solid Solution CeH₂ - CeH₃. *ZPCH* **163**, 125-134 (1989).
64. A. M. Rappe, K. M. Rabe, E. Kaxiras, J. D. Joannopoulos. Optimized pseudopotentials. *Phys. Rev. B* **41**, 1227-1230 (1990).
65. C. Heil, G. B. Bachelet, L. Boeri. Absence of superconductivity in iron polyhydrides at high pressures. *Phys. Rev. B* **97**, (2018).
66. C. Hartwigsen, S. Goedecker, J. Hutter. Relativistic separable dual-space Gaussian pseudopotentials from H to Rn. *Phys. Rev. B* **58**, (1998).

Acknowledgments

Funding: This work was supported by the National Key R&D Program of China (Grant No. 2018YFA0305900), National Natural Science Foundation of China (Grant Nos. 51572108, 51632002, 11974133, 11674122, 11574112, 11474127, and 11634004), National Key Research and Development Program of China (Grant No. 2016YFB0201204), Program for Changjiang Scholars and Innovative Research

Team in University (Grant No. IRT_15R23), and National Fund for Fostering Talents of Basic Science (Grant No. J1103202). A. R. O. thanks Russian Science Foundation (Grant No. 19-72-30043). D. V. S. thanks Russian Foundation for Basic Research, grant No. 19-03-00100 A. The authors express their gratitude to the staffs of BL15U and 4W2 stations of Shanghai and Beijing Synchrotron Radiation Facilities.

Author Contributions:

D. Z., D. V. S. and D. D. contributed equally to this work.

X. H., A. R. O. and T. C. conceived this project. D. Z., D. V. S., and X. H. performed the experiment, D. V. S., D. D. A. R. O. and T. C. prepared theoretical calculations and analysis. X. H., D. Z., D. V. S., A. R. O. and T. C. wrote and revised the paper. All authors discussed the results and offered the useful discussions.

Competing interests: The authors declare no competing interests.

Data and materials availability: All data needed to evaluate the conclusions in the paper are present in the paper and/or the Supplementary Materials. Additional data related to this paper may be requested from the authors.

Supplementary Materials

for

Superconducting praseodymium superhydrides

Di Zhou¹, Dmitrii V. Semenov², Defang Duan¹, Hui Xie¹, Wuha Chen¹, Xiaoli Huang^{1,*}, Xin Li¹,
Bingbing Liu¹, Artem R. Oganov^{2,3,*} and Tian Cui^{1,*}

¹ State Key Laboratory of Superhard Materials, College of Physics, Jilin University, Changchun 130012, China

² Skolkovo Institute of Science and Technology, Skolkovo Innovation Center 143026, 3 Nobel Street, Moscow, Russia

³ International Center for Materials Discovery, Northwestern Polytechnical University, Xi'an, 710072, China

Author Contributions:

E. Z., D. V. S. and D. D. contributed equally to this work.

*Corresponding authors: huangxiaoli@jlu.edu.cn, a.oganov@skoltech.ru and cuitian@jlu.edu.cn

CONTENT

1. Structural information.....	S18
2. Electron and phonon properties of Pr-H phases.....	S23
3. Electrical measurements and superconductivity.....	S24

Structural information

Table S1. Crystal structure of predicted Pr-H phases.

Phase	Pressure, GPa	Lattice parameters	Coordinates			
$F\bar{4}3m$ -PrH ₉	120	$a = 4.960 \text{ \AA}$ $\alpha = \beta = \gamma = 90^\circ$	Pr (4b)	0.50000	0.50000	0.50000
			H (16e)	0.13659	0.13659	0.13659
			H (16e)	-0.11826	-0.11826	-0.11826
			H (4d)	0.75000	0.75000	0.75000
$P6_3/mmc$ -PrH ₉	120	$a = b = 3.566 \text{ \AA}$ $c = 5.577 \text{ \AA}$ $\alpha = \beta = 90^\circ$ $\gamma = 120^\circ$	Pr (2d)	0.33333	0.66667	0.75000
			H (12k)	0.15844	0.31687	0.05586
			H (4f)	0.33333	0.66667	0.34188
			H (2b)	0.00000	0.00000	0.25000
$Fm\bar{3}m$ -PrH ₃	50	$a = 4.808 \text{ \AA}$ $\alpha = \beta = \gamma = 90^\circ$	Pr (4b)	0.50000	0.50000	0.50000
			H (4a)	0.00000	0.00000	0.00000
			H (8c)	0.25000	0.25000	0.25000
$P4/nmm$ -PrH ₃	50	$a = b = 2.884 \text{ \AA}$ $c = 6.099 \text{ \AA}$ $\alpha = \beta = \gamma = 90^\circ$	Pr (2c)	-0.50000	0.00000	0.74831
			H (2c)	-0.50000	0.00000	0.37384
			H (2b)	-0.50000	0.50000	0.50000
			H (2c)	0.00000	0.50000	-0.09063
$Fm\bar{3}m$ -PrH	50	$a = 4.338 \text{ \AA}$ $\alpha = \beta = \gamma = 90^\circ$	Pr (4b)	0.50000	0.50000	0.50000
			H (4a)	0.00000	0.50000	0.50000

Table S2. Experimental parameters of DACs.

#cell	Pressure of heating, GPa	Gasket	Sample size, μm	Composition/load
Z1	110	W	17/30	Pr/BH ₃ NH ₃
Z2	40	W	25	Pr/H ₂
Z3 (sample 1)	100/120	W	35/50	Pr/BH ₃ NH ₃
Z4 (sample 2)	114	W	50	Pr/BH ₃ NH ₃

Table S3. Experimental cell parameters and volumes of lower praseodymium hydrides along with calculated cell volumes (V_{DFT}).

P (GPa)	$Fm\bar{3}m$ -PrH ₃ (Z=4)			$Fm\bar{3}m$ -PrH (Z=4)			P (GPa)	$P4/nmm$ -PrH ₃ (Z=2)			
	a (\AA)	V (\AA^3)	V_{DFT} (\AA^3)	a (\AA)	V (\AA^3)	V_{DFT} (\AA^3)		a (\AA)	c (\AA)	V (\AA^3)	V_{DFT} (\AA^3)
10	5.196(0)	140.31(2)	140.11	4.815(1)	111.63(6)	105.29	53	2.795(2)	6.264(2)	48.94(9)	50.18
14	5.133(0)	135.25(1)	135.38	4.750(1)	107.17(6)	101.83	48	2.807(1)	6.291(2)	49.55(5)	51.18
20	5.061(1)	129.69(7)	129.92	4.653(1)	100.73(6)	97.412	43	2.819(2)	6.318(2)	50.21(9)	52.27
26	5.026(1)	127.02(8)	125.41	4.607(0)	97.81(3)	93.35	17	2.965(2)	6.645(3)	58.41(8)	61.93
29	4.991(1)	124.39(8)	123.17	4.571(0)	95.52(1)	91.19					
35	4.938(0)	120.42(2)	119.78	4.520(0)	92.37(2)	88.52					
39	4.909(1)	118.34(6)	117.00	4.473(1)	89.48(5)	86.40					
43	4.878(0)	116.08(1)	115.22								
49	4.837(1)	113.22(7)	112.15								
53	4.811(0)	111.38(4)	110.70								

Table S4. Experimental cell parameters and volumes of two praseodymium superhydrides along with calculated cell volumes (V_{DFT}).

P (GPa)	$P6_3/mmc\text{-PrH}_9$ ($Z=2$)				$F\bar{4}3m\text{-PrH}_9$ ($Z=4$)		
	a (Å)	c (Å)	V (Å ³)	V_{DFT} (Å ³)	a (Å)	V (Å ³)	V_{DFT} (Å ³)
105	3.635(1)	5.492(3)	62.83(8)	63.33	5.024(1)	126.77(8)	126.00
111	3.615(1)	5.479(0)	62.05(4)	62.57	4.999(1)	124.93(5)	124.14
114	3.604(1)	5.473(3)	61.55(8)	62.01	4.987(1)	123.99(7)	123.45
118	3.595 (1)	5.468(4)	61.01(9)	61.57	4.976(1)	123.18(9)	122.40
121	3.588(1)	5.458 (4)	60.84(9)	61.19	4.965(1)	122.42(5)	121.63
123	3.590(1)	5.461(3)	60.94(6)	60.93	4.967(1)	122.52(9)	121.12
124	3.587 (1)	5.458(4)	60.83(9)	60.76	4.965(1)	122.41(5)	120.96
129	3.580 (1)	5.441(4)	60.49(9)	60.23	4.947(1)	121.07(7)	123.63

Table S5. Reference EoS parameters of pure elemental Pr in the modified universal equation of state (MUEOS) as below:

$$\ln H = \ln B_0 + \eta(1 - x) + \beta(1 - x)^2 \quad \text{S1}$$

where $x^3 = \frac{V}{V_0}$ is the volume compression, $\eta = 1.5(B'_0 - 1)$, and $H = Px^2/[3(1 - x)]$. V_0 , B_0 , B'_0 are the atomic volume, isothermal bulk modulus and the first pressure derivative of the bulk modulus at the ambient pressure.

	$dhcp\text{-Pr}$	$C2/m\text{-Pr}$	$Cmcm\text{-Pr}$
V_0 (GPa)	34.538	34.538	29.012
K_0 (GPa)	27.16(2)	27.16(4)	24.73(1)
K'	0.096(4)	1.424(5)	1.933(3)
β	39.88(2)	25.25(6)	22.35(1)

Table S6. Calculated EoS parameters of 3rd Birch–Murnaghan equation for all studied Pr-H phases. For both PrH_9 V_0 corresponds to 100 GPa, for both PrH_3 and PrH correspond to 0 GPa.

	$F\bar{4}3m\text{-PrH}_9$	$P6_3/mmc\text{-PrH}_9$	$Fm\bar{3}m\text{-PrH}_3$	$P4/nmm\text{-PrH}_3$	$Fm\bar{3}m\text{-PrH}$
V_0 (GPa)	31.91	31.68	37.73	32.12	32.07
K_0 (GPa)	475.88	398.19	113.19	150.20	53.04
K'	5.507	19.74	3.047	2.09	4.122

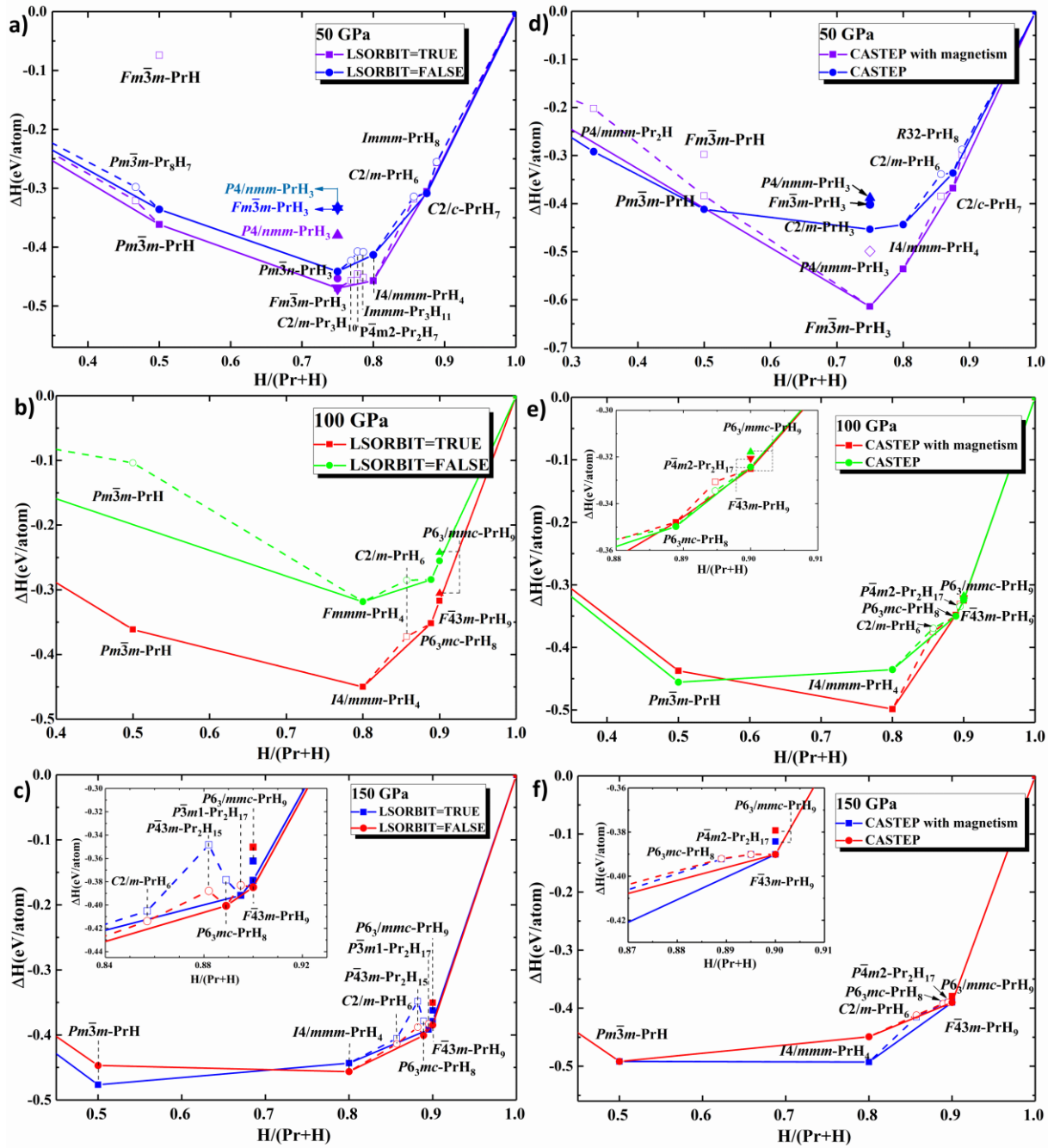


Fig. S1. Calculated convex hulls for Pr-H system at various pressures. Convex hulls for Pr-H system with and without spin-orbital and magnetic corrections calculated in USPEX at (a) 50 GPa (b) 100 GPa and (c) 150 GPa. The convex hulls of Pr-H systems calculated in AIRSS at (d) 50 GPa (e) 100 GPa and (f) 150 GPa. Inset shows the stability of hexagonal PrH₈ and cubic PrH₉.

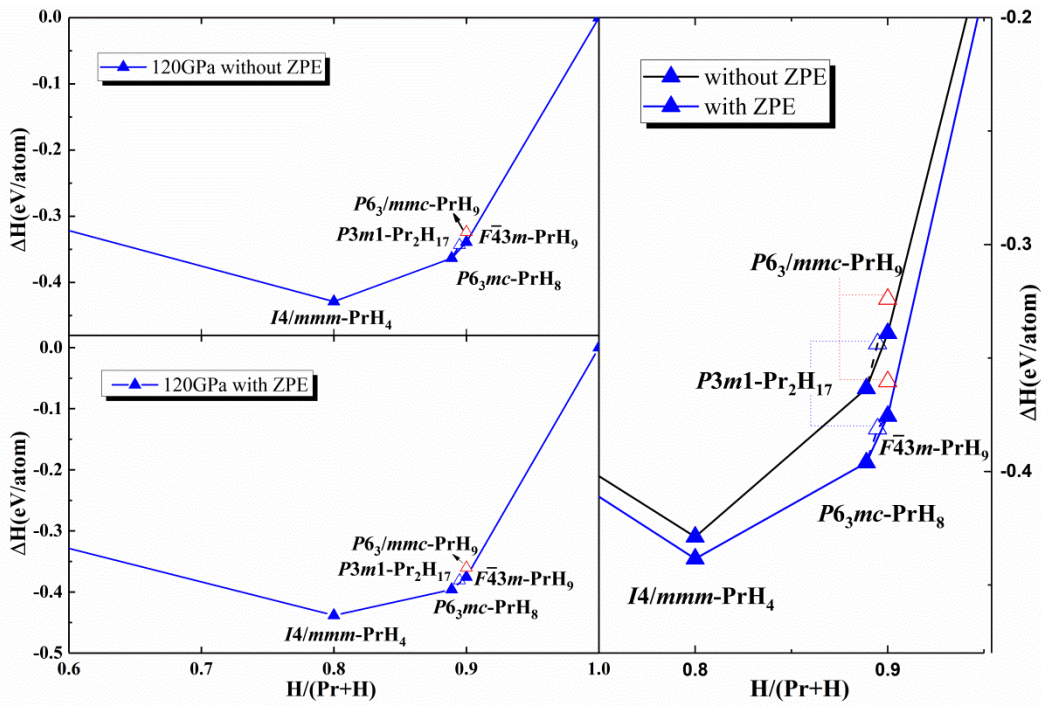


Fig. S2. Convex hulls without and with ZPE correction of discovered praseodymium hydrides at 120 GPa.

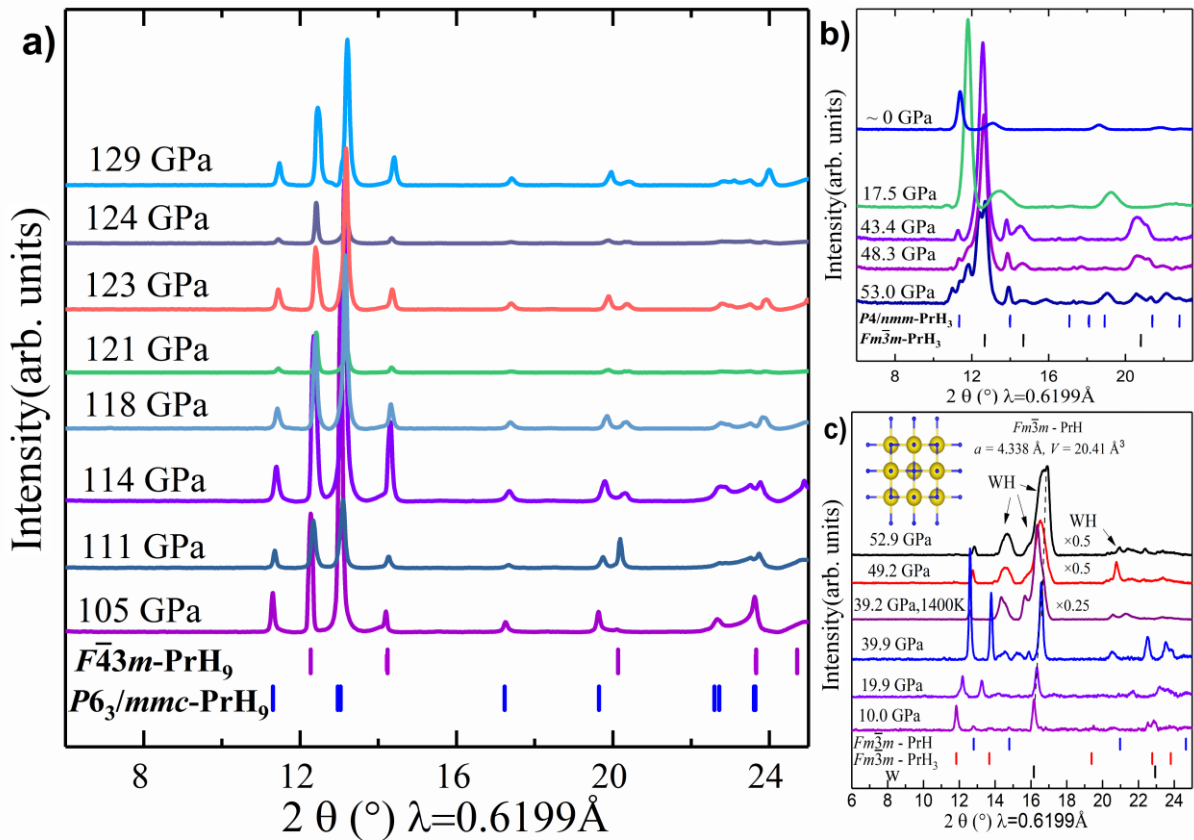


Fig. S3. Experimental XRD patterns dependence of pressure in the range of 0-130 GPa. (a) Experimental XRD patterns for the mixture of PrH_9 in the range of 129-105 GPa. (b) The XRD patterns upon decompression. (c) The selected XRD patterns during the compressing process of Pr with pure H_2 . $Fm\bar{3}m\text{-PrH}_3$ and $Fm\bar{3}m\text{-PrH}$ were synthesized at low pressure, after heating the peaks of $Fm\bar{3}m\text{-PrH}$ disappeared.

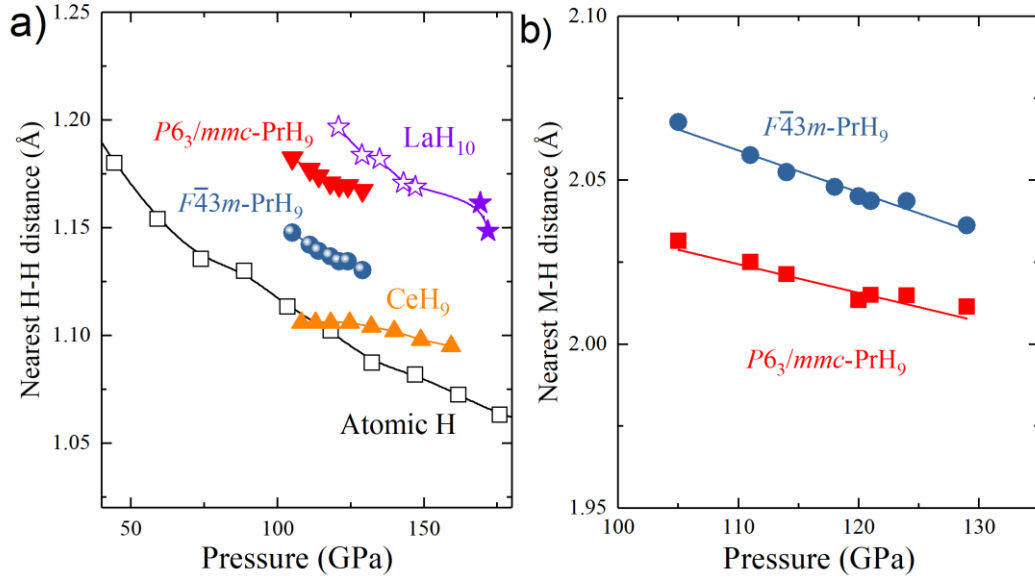


Fig. S4. Pressure dependence of the nearest H-H distances and Nearest Pr-H distances from experimental cell parameters. (a) Pressure dependence of the nearest H-H distances for two PrH₉, LaH₁₀ (Ref. 5), CeH₉ (Ref. 39), and atomic H (62). (b) Nearest Pr-H distances as a function of pressure calculated from experimental cell parameters.

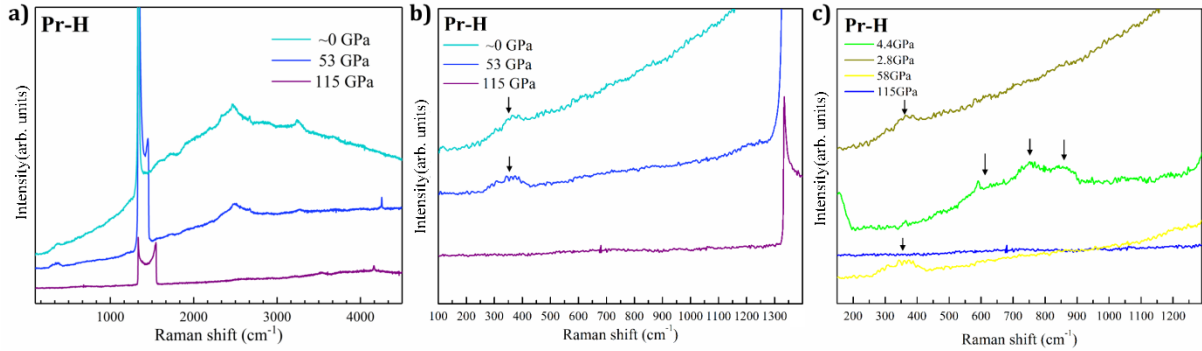


Fig. S5. Raman spectra of Z1 cell under decompression. After diamond broken, there was a small peak at 340 cm⁻¹, which might response to the non-stoichiometric PrH_{2+x} phases according to the analogy with CeH_{2+x} (63).

Electron and phonon properties of Pr-H phases

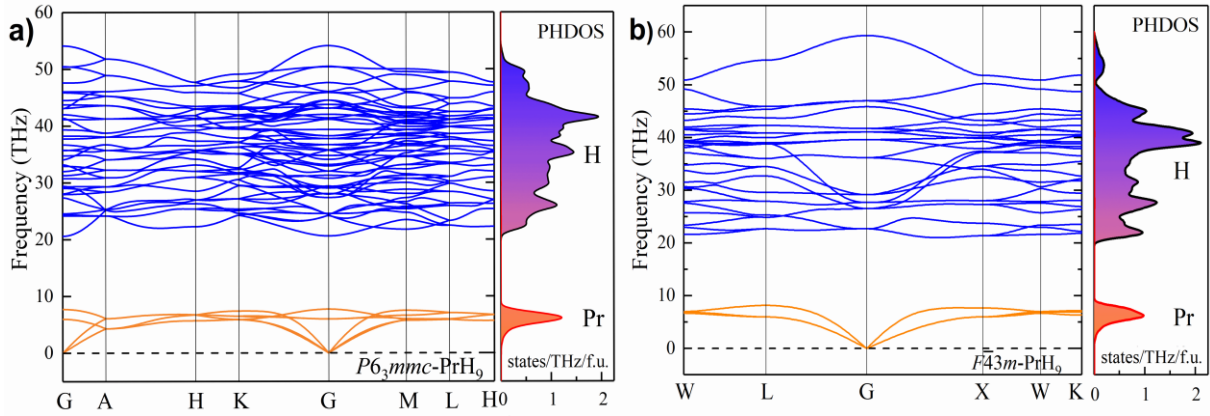


Fig. S6. Calculated phonon density of states and band structure for (a) $P6_3/mmc$ -PrH₉ and (b) $F\bar{4}3m$ -PrH₉ at 120 GPa that were used to calculate zero-point energy correction for Pr-H convex hull.

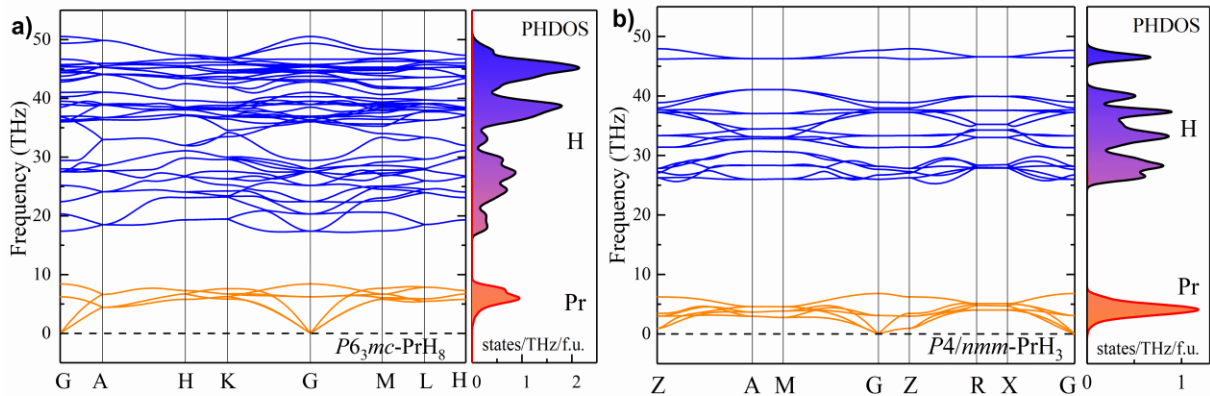


Fig. S7. Calculated phonon density of states and band structure for (a) $P6_3mc$ -PrH₈ at 120 GPa and (b) $P4/nmm$ -PrH₃ at 50 GPa.

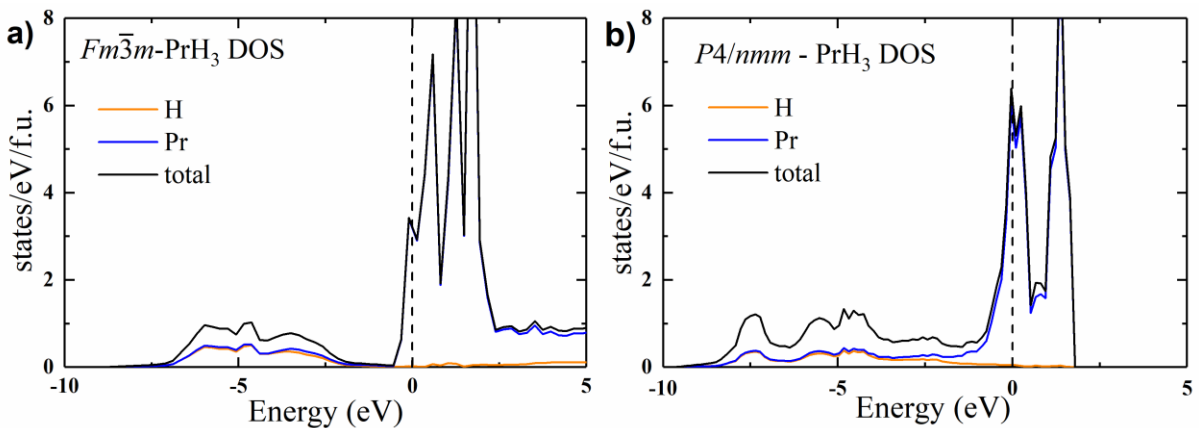


Fig. S8. Electron density of states for (a) cubic PrH₃ and (b) $P4/nmm$ -PrH₃ at 30 GPa (per f.u.). DOS(E_F) caused mostly by Pr d,f -electrons and has very high value in both cases that may have negative effect on SC properties.

Electrical measurements and superconductivity

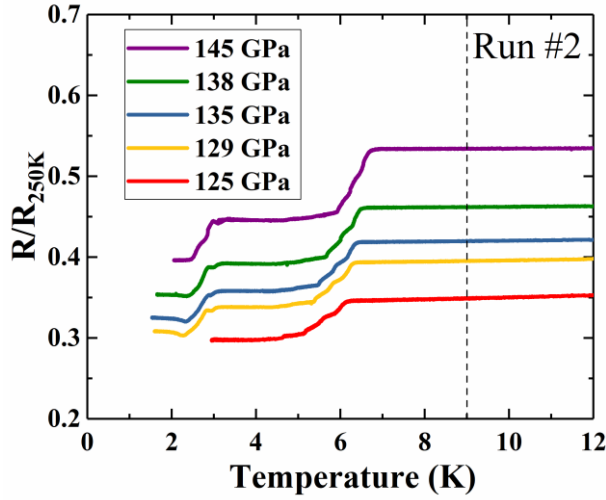


Fig. S9. Enlarged figure of electrical resistance measurements of PrH₉ in sample 2.

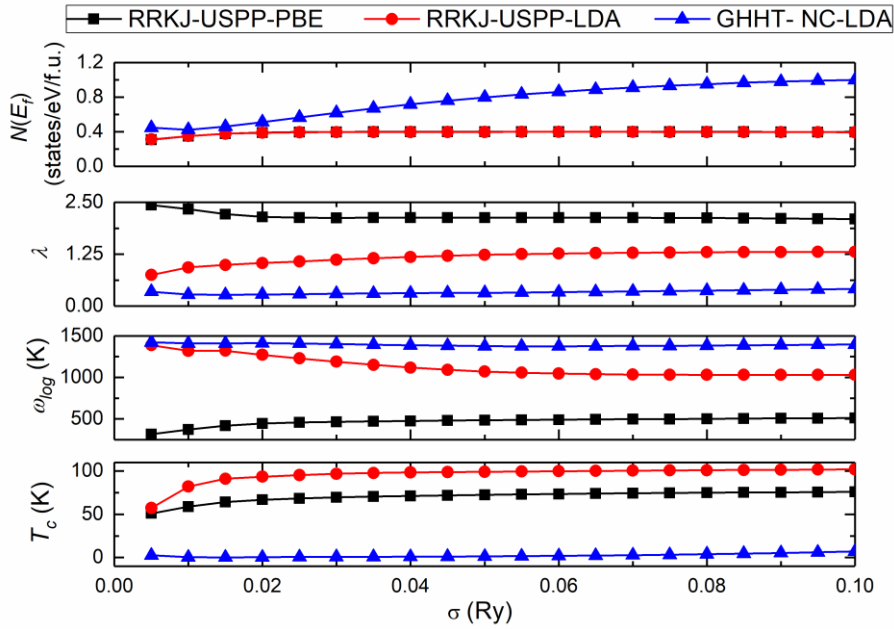


Fig. S10. Calculated superconducting parameters of $F\bar{4}3m$ -PrH₉ at 120GPa as a function of electronic smearing σ and the pseudopotential. Density of electronic states $N(E_f)$ (first panel), EPC coefficient λ (second panel), logarithmic frequency ω_{log} (third panel), and Allen-Dynes modified McMillan critical temperature T_c (fourth panel) of $F\bar{4}3m$ -PrH₉ at 120GPa as a function of electronic smearing σ and the pseudopotential

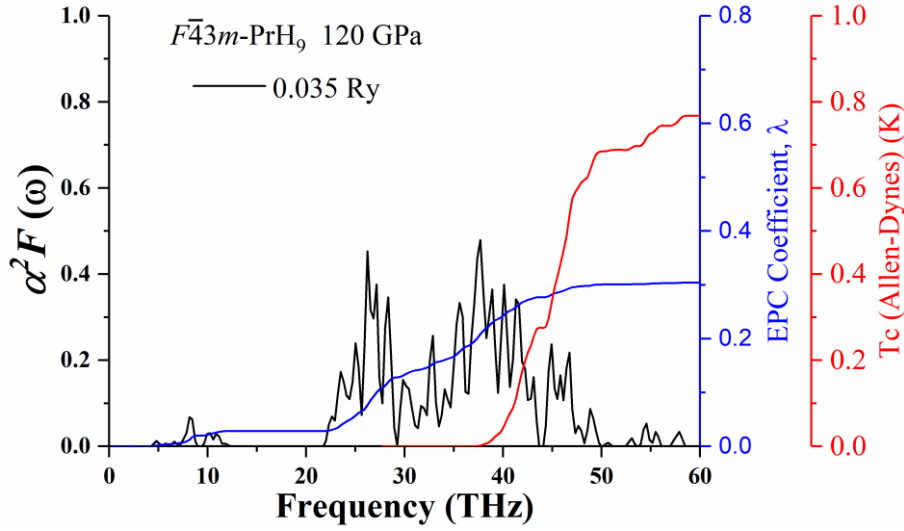


Fig. S11. Eliashberg spectral functions, the electron-phonon integral $\lambda(\omega)$ and critical transition temperature $T_c(\omega)$ calculated at 120 GPa for cubic PrH₉ with $\sigma = 0.035$ Ry.

We calculated superconducting parameters of cubic PrH₉ (120 GPa) with different pseudopotentials (PPs) including the ultrasoft Rappe-Rabe-Kaxiras-Joannopoulos (64, 65) (RRKJ-PBE, RKKL-LDA) and the norm-conserving Goedecker-Hartwigsen-Hutter-Teter (66) (GHHT-NC-LDA) pseudopotentials. The first Brillouin zone was sampled using $6 \times 6 \times 6$ q-points mesh, and a denser $24 \times 24 \times 24$ k-points mesh was used to calculate the electron wave functions. A kinetic-energy cutoff of 80 Ry for RRKJ and 90 Ry for GHHT was applied. Furthermore, we use Allen-Dynes modified McMillan formula with Coulomb pseudopotential $\mu^* = 0.1$ to estimate T_c . The superconducting state computed with ultrasoft RKKJ PPs lead to $T_c(\text{McM}) > 60$ K. But the experiment clearly indicated absence of SC transition between 50 and 100 K indicating that ultrasoft RKKJ PPs is not suitable for Pr-H system. Calculations with Norm-Conserving GHHT (LDA) pseudopotential with electronic smearing $\sigma = 0.035$ Ry gave $\lambda < 0.3$ and $T_c < 1$ K., which does not contradict the experimental data.

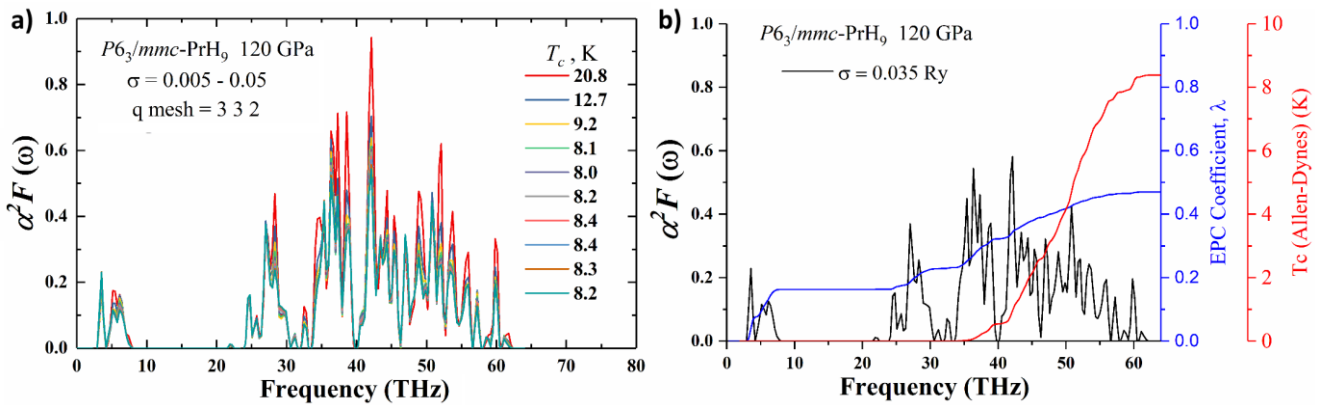


Fig. S12. A series of Eliashberg spectral functions calculated at 120 GPa for hexagonal PrH₉ with (a) q mesh = 3 3 2 and (b) the electron-phonon integral $\lambda(\omega)$ and critical transition temperature $T_c(\omega)$ with $\sigma = 0.035$ Ry. This diagram illustrates the high sensitivity of the T_c calculations (by Allen-Dynes modified McMillan formula, $\mu^*=0.1$) due to quite complex structure of DOS near the Fermi level.

We continue to calculate superconducting parameters of another superhydrides $P6_3/mmc$ -PrH₉ using norm-conserving GHHT (LDA) pseudopotential, as shown in Fig. S12, where the electron-phonon interaction should be much stronger. A larger T_c of 8.4 K at 120 GPa is obtained, which are in good agreement with the experimental data.